

mW to the film. For smaller or larger spots, the power was decreased or increased approximately in proportion to the diameter of the laser spot focused on the tissue. The absorption coefficient of the EVA film, measured by Fourier transform infrared spectroscopy as well as by direct transmission, was 200 cm^{-1} at the laser wavelength ($10.6 \text{ }\mu\text{m}$). Because $>90\%$ of the laser radiation was absorbed within the thermoplastic film, little direct heating of the tissue specimen by the laser occurred. The glass slide provided a large heat sink that confined the full-thickness transient focal melting of the thermoplastic material to the targeted region. The focally molten plastic wet the targeted tissue. After cooling and recrystallization, the film formed a local surface bond to the targeted tissue that was stronger than the adhesion forces of the tissue to the slide. The film and targeted cells were removed from the tissue specimen, resulting in focal microtransfer of the targeted tissue to the film surface.

15. For PCR, the transfer film and adherent cells were immediately resuspended in $40 \text{ }\mu\text{l}$ of 10 mM tris-HCl (pH 8.0), 1 mM EDTA, 1% Tween-20, and proteinase K (0.1 mg/ml) and incubated overnight at 37°C . The mixture was boiled for 10 min to inactivate the proteinase K. The tubes were briefly spun (1000 rpm , 1 min) to remove the film, and $0.5 \text{ }\mu\text{l}$ of the supernatant was used for PCR. For the most efficient tissue recovery, the transfer film was initially applied to the tissue section as a circular disk (diameter 0.5 cm). After LCM transfer, the disk was placed into a well in a 96-well microtiter plate containing $40 \text{ }\mu\text{l}$ of extraction buffer. The oligonucleotide primers for the polymorphic DNA markers were purchased from Research Genetics (Huntsville, AL). Loci were *D8S136* and *D8S339* located on chromosome 8p, *D17S855* on chromosome 17q21, *D11S449* on chromosome 11q13, *D9S171* on chromosome 9p, specific primers for exon 2 of the VHL gene, and specific primers for *M. tuberculosis*. All PCR reactions used incorporation of [^{32}P]deoxycytidine triphosphate for visualization of product except amplification of *M. tuberculosis*, which was visualized by ethidium bromide staining.

16. M. Emmert-Buck *et al.*, *Cancer Res.* **55**, 2959 (1995).
17. For RT-PCR, total RNA was extracted from tissue after LCM by means of a modification of an RNA microisolation protocol (Stratagene). Volumes were proportionally adjusted downward, and a 10-fold increase in glycogen carrier (10 ng/ml) was used in all precipitation steps. After initial recovery and resuspension of the RNA pellet, a deoxyribonuclease (DNase) step was performed for 3 hours at 37°C using DNase (10 U/ml ; GenHunter, Nashville, TN) in the presence of 4 U of RNase Inhibitor (Perkin-Elmer), followed by reextraction of the RNA. The resuspended RNA was reverse-transcribed using $5 \text{ }\mu\text{M}$ random hexamer primers (Perkin-Elmer), 250 mM deoxynucleotide triphosphate, and 100 U of reverse transcriptase (MMLV, GenHunter). PCR was performed with specific actin or PSA primers, and the products were subjected to denaturing electrophoresis gel analysis.
18. S. Meyers, R. F. Bonner, M. M. Rodrigues, E. J. Ballantine, *Ophthalmology* **90**, 563 (1983).
19. J. Walsh, T. J. Flotte, R. R. Anderson, T. F. Deutsch, *Lasers Surg. Med.* **8**, 108 (1988).
20. P. O'Connell, V. Pekkel, S. Fuqua, C. K. Osborne, D. C. Allred, *Breast Cancer Res. Treat.* **32**, 5 (1994).
21. Z. Zhuang, M. J. Merino, R. F. Chuaqui, L. A. Liotta, M. R. Emmert-Buck, *Cancer Res.* **55**, 467 (1995).
22. D. Page, W. D. Dupont, L. W. Rogers, M. S. Rados, *Cancer* **55**, 2698 (1985).
23. J. McNeal and D. G. Bostwick, *Hum. Pathol.* **17**, 64 (1986).
24. We are currently optimizing thinner, smoother transfer films and finer laser activation, which may allow for reproducible transfer of targeted single cells (R. F. Bonner *et al.*, in preparation).
25. We thank S. K. Apple, J. P. Struewing, W. M. Linehan, C. D. Vocke, G. Oliver, A. Lash, M. J. Roth, M. J. Merino, P. H. Duray, I. A. Lubensky, L. V. Debelenko, V. E. Norman, and A. Coleman for tissue samples, technical support, or editing of the manuscript.

30 May 1996; accepted 16 September 1996

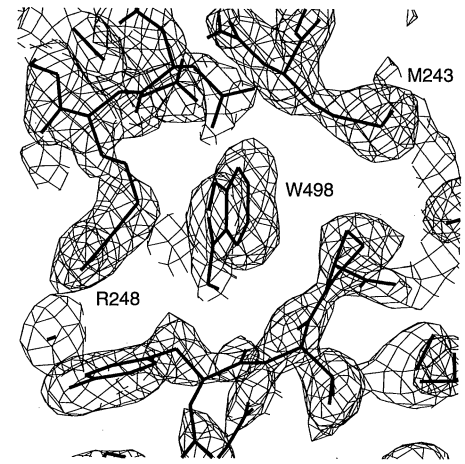


Fig. 1. Electron density at the p53-SH3 domain interface, contoured at 1.2σ (25). The $(2|F_{\text{obs}}| - |F_{\text{calc}}|)$ Fourier synthesis was calculated at 2.2 \AA resolution using phases calculated after omitting the interface residues shown, and subjecting the model to simulated annealing refinement from 3000 K . Met²⁴³ and Arg²⁴⁸ of p53 and Trp⁴⁹⁸ of 53BP2 are labeled.

null mice (9) do not exhibit the tumor-prone phenotype of p53-null mice (10), suggesting the existence of additional mediators of p53's tumor suppressing effects.

In addition to DNA binding, several protein binding activities have been described for p53 (1). Among these, the binding of the 53BP2 protein, which was identified by its ability to bind the core domain of p53 in a yeast two-hybrid screen (11), is disrupted by alanine substitutions at several of the frequently mutated amino acids of p53 (11). To help investigate the significance of the 53BP2-p53 interaction, we have determined the 2.2 \AA crystal structure of the complex containing the p53 core domain and a 229-residue COOH-terminal domain of 53BP2 (Fig. 1 and Table 1). This complex forms with a dissociation constant of $\approx 30 \text{ nM}$ as determined by surface plasmon resonance measurements (12).

The 53BP2 COOH-terminal domain (residues 291 to 519) contains four ankyrin repeats (13), each about 30 residues long, and a Src-homology-3 (SH3) domain (14)—two distinct structural motifs that mediate protein-protein interactions in diverse regulatory molecules. In the crystal structure of the 53BP2-p53 complex, the ankyrin repeats and the SH3 domain form a single structural domain as they pack extensively against each other (Fig. 2, A and B).

The p53 core domain structure in the complex is essentially identical to the crystal structures of free and DNA-bound p53 (15), consisting of a β sandwich that serves as a scaffold for two large loops (the L2 and L3 loops) and a loop-sheet-helix motif (H2

Structure of the p53 Tumor Suppressor Bound to the Ankyrin and SH3 Domains of 53BP2

Svetlana Gorina and Nikola P. Pavletich

Mutations in the p53 tumor suppressor are among the most frequently observed genetic alterations in human cancer and map to the 200-amino acid core domain of the protein. The core domain contains the sequence-specific DNA binding activity and the *in vitro* 53BP2 protein binding activity of p53. The crystal structure of the p53 core domain bound to the 53BP2 protein, which contains an SH3 (Src homology 3) domain and four ankyrin repeats, revealed that (i) the SH3 domain binds the L3 loop of p53 in a manner distinct from that of previously characterized SH3-polyproline peptide complexes, and (ii) an ankyrin repeat, which forms an L-shaped structure consisting of a β hairpin and two α helices, binds the L2 loop of p53. The structure of the complex shows that the 53BP2 binding site on the p53 core domain consists of evolutionarily conserved regions that are frequently mutated in cancer and that it overlaps the site of DNA binding. The six most frequently observed p53 mutations disrupt 53BP2 binding *in vitro*. The structure provides evidence that the 53BP2-p53 complex forms *in vivo* and may have a critical role in the p53 pathway of tumor suppression.

The p53 tumor suppressor pathway (1, 2) has a central role in suppressing neoplastic transformation as it can respond to DNA damage by inducing cell cycle arrest (3) or

apoptosis (4, 5). The cell cycle arrest is mediated, at least in part, by p53's sequence-specific DNA binding (6) and transactivation functions (7), which can induce the expression of the p21(Cip1-WAF1) cyclin-dependent kinase inhibitor, arresting the cell cycle (8). However, p21-

Cellular Biochemistry and Biophysics Program, Memorial Sloan-Kettering Cancer Center, New York, NY 10021, USA.

helix). The two loops bind a zinc atom, and together with the H2 helix form a continuous surface at one end of the β sandwich. This surface holds the key to understanding p53's function and its inactivation in tumors because it consists of evolutionarily conserved regions of p53 [conserved boxes III, IV, and V (15)] to which most of the tumorigenic mutations map (15). 53BP2 uses its fourth ankyrin repeat and its SH3 domain to bind two adjacent, but discontinuous, portions of this surface (Fig. 2, A and B). A β hairpin from the fourth ankyrin repeat contacts the L2 loop of p53 (conserved box III), whereas the peptide binding groove of the SH3 domain, which makes significantly more contacts, interacts with the L3 loop of p53 (conserved box IV). The site of 53BP2 binding overlaps the site of DNA binding (Fig. 2, C and D) (15).

The binding of the 53BP2 SH3 domain to the L3 loop of p53 differs from that observed in canonical SH3-polyproline peptide (PXXP ligand, where P stands for proline) complexes in several ways (16, 17). In the 53BP2-p53 complex two segments of the p53 L3 loop bind the groove of the SH3 domain, whereas in SH3-PXXP complexes only a single extended peptide binds (Fig. 3A) (16, 17). Furthermore, in the 53BP2-p53 complex, the positions and orientations of the interacting groups are determined by the global structure of the p53 core domain, whereas in SH3-PXXP complexes the steric and hydrogen bonding complementarity is provided by the peptide adopting a left-handed polyproline-II helix conformation (16, 17).

The L3 loop of p53 forms a rigid hairpin structure that is stabilized by multiple intramolecular hydrogen bonds and by zinc coordination (15). The NH_2 -terminal segment of the L3 hairpin (residues 241 to 243) occupies a position on the SH3 peptide-binding groove similar to the $\text{P}_0 - \text{P}_{-1} - \text{P}_{-2}$ residues of a PXXP ligand (Fig. 3A), and it makes contacts analogous to those in canonical SH3-PXXP complexes. The Met^{243} side chain of p53 binds the hydrophobic pocket of the SH3 domain (analogous to the P_0 hydrophobic residue of a PXXP ligand), and the backbone carbonyl of Ser^{241} hydrogen bonds to the Trp^{498} side chain of 53BP2 (Fig. 3B). The COOH-terminal segment of the L3 hairpin (residues 247 and 248) is juxtaposed to the NH_2 -terminal segment and also binds in the SH3 groove, but it is positioned in a manner not seen in other SH3 complexes (Fig. 3A). In this region, the Asn^{247} side chain of p53 hydrogen bonds to the Tyr^{469} hydroxyl group, and the Arg^{248} side chain makes charge stabilized hydrogen bonds to the Asp^{475} and Glu^{476} side chains from a segment of the SH3 domain called the RT-loop (site of critical residues in the

Src-SH3 domain) (Fig. 3B). These interactions are augmented by hydrogen bonds made by the backbone carbonyl groups of Asn^{247} and Arg^{248} of p53 (Fig. 3B). The significance of the Arg^{248} -RT-loop interactions is underscored by the dependence of SH3-PXXP complexes on RT-loop contacts

for binding and specificity (16, 17), and by the observation that Arg^{248} is the most frequently mutated amino acid of p53 (2). In addition to the peptide binding groove of the SH3 domain, a loop consisting of residues 490 to 497 (referred to as the n-src loop), which contains a three-residue insertion

Table 1. Statistics from the crystallographic analysis.

Data set	Data collection				
	Native-1	Native-2	Hg	Pb	
Resolution (Å)	2.5	2.2	2.8	3.0	
Observations	115005	220654	33660	16576	
Unique reflections	17423	30230	14074	9717	
Data coverage (%)	82.3	99.1	91.6	78.2	
R_{sym}^* (%)	3.7	5.7	6.2	7.9	
MIR analysis (20.0 to 3.2 Å)					
Isomorphous difference†			0.20	0.21	
Phasing power‡			2.2	0.9	
Refinement statistics					
Atoms					
Resolution	Reflections§	Protein	Water	R_{int}	$R_{\text{free}}^{\text{¶}}$
7.0–2.2 Å	25435	3066	275	0.205	0.286
rmsd#	Bond lengths: 0.013 Å		Bond angles: 1.64°		B factors: 3.17 Å ²

* $R_{\text{sym}} = \sum_h \sum_i |I_{h,i} - \bar{I}_h| / \sum_h \sum_i I_{h,i}$, for the intensity (I) of i observations of reflection h . †Mean isomorphous difference = $\sum |F_{\text{PH}} - F_{\text{P}}| / \sum F_{\text{PH}}$, where F_{PH} and F_{P} are the derivative and native structure factors, respectively. ‡Phasing power = $|F_{\text{H}_2\text{O}}| / (|F_{\text{PH}} - F_{\text{P}}|)^{1/2}$. §Reflections with $|F| > 2\sigma$. ¶ R_{free} factor = $\sum |F_{\text{O}} - F_{\text{C}}| / \sum |F_{\text{O}}|$, where F_{O} and F_{C} are the observed and calculated structure factors, respectively. ¶ R_{free} calculated with 10 percent of the data chosen randomly and omitted from simulated annealing refinement from 3000 K. #Root-mean-square deviations from ideal geometry, and root-mean-square variation in the B-factors of bonded atoms.

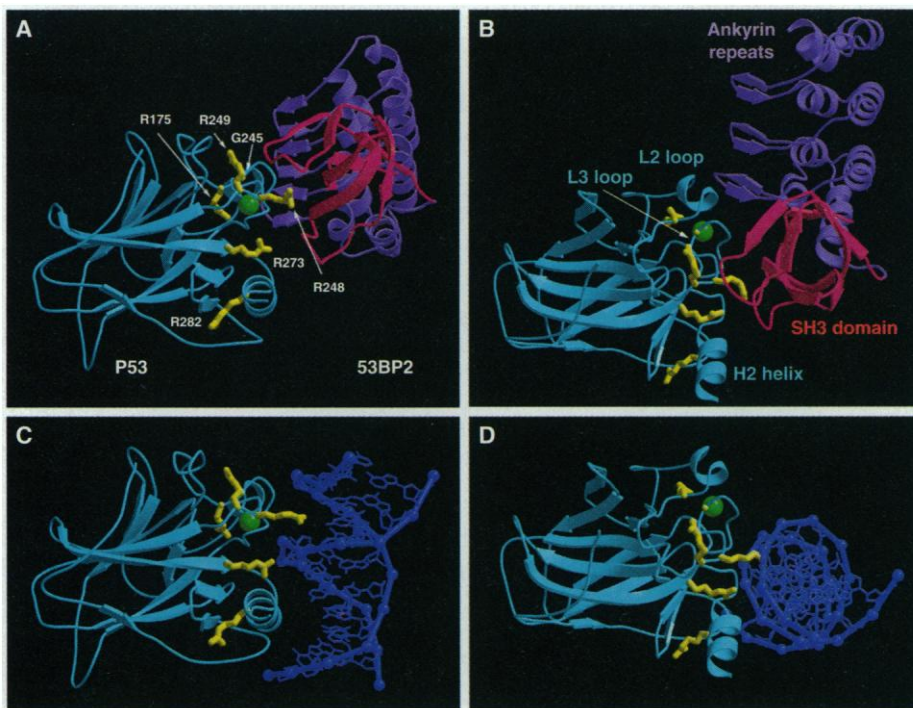


Fig. 2. Comparison of the p53-53BP2 and p53-DNA (15) complexes in two orthogonal views (rotated by 90° about the x -axis). The six most frequently mutated amino acids of p53, highlighted in yellow, are at or near both the 53BP2 and DNA interfaces. (A and B) The 53BP2 SH3 domain (red) binds the L3 loop, while the fourth ankyrin repeat (magenta) binds the L2 loop of the p53 core domain (cyan). The zinc atom of p53 is shown as a green sphere. (C and D) Comparison with the p53-DNA (blue) complex (15) in the same p53 orientations as (A and B). Abbreviations for the amino acid residues are: A, Ala; C, Cys; D, Asp; E, Glu; F, Phe; G, Gly; H, His; I, Ile; K, Lys; L, Leu; M, Met; N, Asn; P, Pro; Q, Gln; R, Arg; S, Ser; T, Thr; V, Val; W, Trp; Y, Tyr.

compared to the SH3 consensus, is also in close proximity to p53 and is likely to play a role in binding, although its partial disorder in the crystal structure makes this difficult to evaluate. Six of the eight amino acids in this loop are carboxylic acids, and they are positioned near Arg²⁷³ of p53 (Fig. 2, A and B).

The 53BP2 SH3 sequence aligns with the overall SH3 consensus well, except that a peptide-binding groove Tyr residue, conserved in almost all the SH3 domains [Tyr¹⁸⁶ in c-Crk (17)], is replaced by Leu⁵¹⁴ in 53BP2 (Fig. 3A). The functional significance of this substitution is that in canonical SH3-PXXP complexes the Tyr side chain makes van der Waals contacts to the hydrophobic P₀ residue of the PXXP peptide (16, 17), but in the 53BP2-p53 complex, the Met²⁴³ of p53 that binds in this region is bulkier than the P₀ residues of canonical PXXP ligands (Pro, Val, Leu), and it would not fit well in the binding site if 53BP2 had a Tyr residue at position 514 (Fig. 3A).

The crystal structure revealed that an individual ankyrin repeat has a novel L-

shaped structure consisting of a β hairpin (bottom of the letter L) followed by two α helices that pack in an antiparallel fashion (stem of the letter L, Fig. 4A). The β hairpin is connected to the first helix via a one-residue linker, with the plane of the β sheet being perpendicular to the helix axes. Neighboring repeats pack via their hairpins to form a continuous antiparallel β sheet, and via their helix pairs to form helix bundles (Fig. 4A). The folding of the ankyrin motif structure thus depends on the presence of neighboring repeats, and it is unlikely that an isolated repeat can fold stably.

The β hairpin consists of hydrophilic amino acids and is mostly solvent exposed. Its structure relies on the formation of a continuous antiparallel β sheet with neighboring repeats, as well as on extensive intra- and inter-repeat side chain hydrogen bonds (Fig. 4A). The two α helices of the repeat are connected by a tight turn, and pack in an antiparallel fashion. Pairs of α helices from adjacent ankyrin repeats pack in parallel forming four-helix bundles with a left-handed twist (Fig. 2, A and B). Conserved residues of the ankyrin motif (13) in the helical regions have conserved structural roles in the four repeats. These residues often help initiate α helices (residues 362, 373, 395, 429, and 442, Fig.

4B), Gly residues help terminate helices (residues 338, 371, 383, and 416, Fig. 4B), the highly conserved His residues contribute to inter-repeat stabilization through hydrogen bond networks (residues 365 and 398, Fig. 4, A and B), and hydrophobic residues contribute to intra- and inter-repeat packing (Fig. 4B).

In the 53BP2-p53 complex, the fourth ankyrin repeat uses its β hairpin to bind to a portion of p53's L2 loop immediately after the zinc ligands (H1 helix). At the turn of the ankyrin β hairpin, the 53BP2 Ser⁴²⁵ backbone carbonyl makes a pair of hydrogen bonds with the p53 Ser¹⁸³ side chain and backbone amide (Fig. 4C). The turn of the hairpin contains a one-residue insertion compared to the ankyrin consensus, and the structure suggests that this extra residue is important for steric and hydrogen bond complementarity in this region of the interface. An additional hydrogen bond is made between the Met⁴²² backbone carbonyl of 53BP2 and the His¹⁷⁸ side chain of p53 (Fig. 4C). The remaining contacts are van der Waals in nature, and involve Tyr⁴²⁴ from the turn and Met⁴²² and Met⁴²⁷ from the face of the β hairpin of 53BP2, and His¹⁷⁸, His¹⁷⁹, Ser¹⁸², and Arg¹⁸¹ of p53 (Fig. 4C).

Ankyrin repeats mediate macromolecular recognition in diverse regulatory pro-

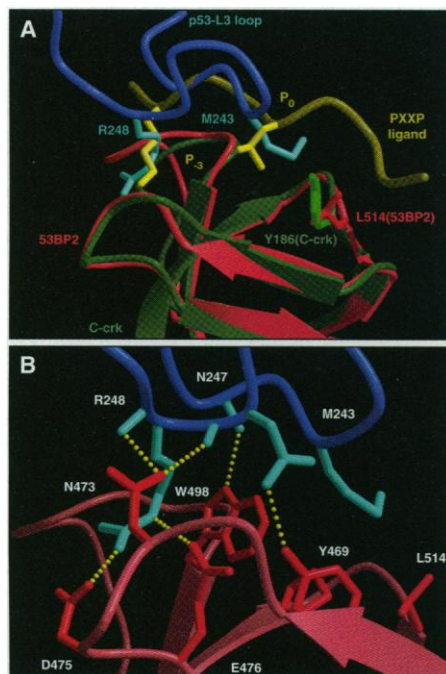


Fig. 3. The 53BP2 SH3 domain uses its peptide binding groove, characterized in SH3-PXXP peptide complexes, to bind the rigid L3 loop of p53. (A) Comparison of the 53BP2 SH3-p53 interface with that of the c-Crk SH3 bound to a PXXP peptide derived from the C3G protein (17). 53BP2 is in red; p53 in blue; C-crK in green; the C3G PXXP peptide in yellow; and the some of the side chains discussed in the text are colored in brighter tones. (B) Side chains and backbone groups of the L3 loop of p53 (blue) make multiple van der Waals and hydrogen bond contacts (yellow dotted lines) to the peptide binding groove of the 53BP2 SH3 domain (red). Only interacting side chains are shown; orientation is similar to that of Fig. 3A.

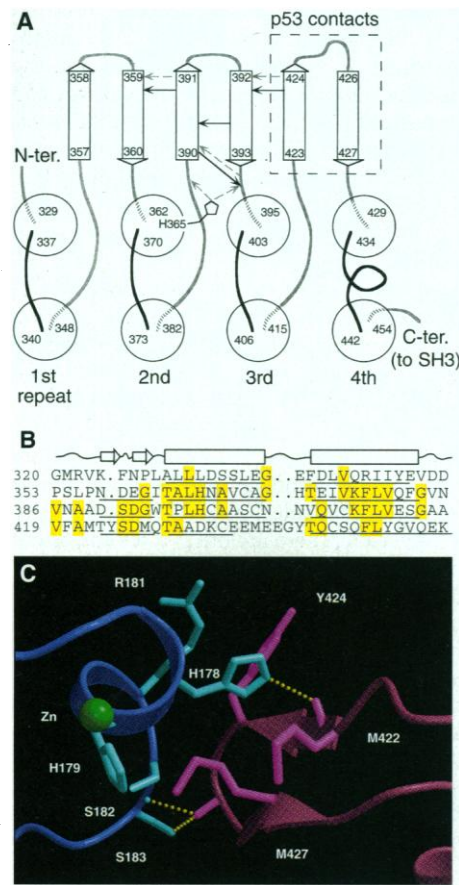


Fig. 4. An ankyrin repeat forms an L-shaped structure that consists of a β hairpin and two α helices. (A) Topological diagram of the secondary structure elements of the 53BP2 ankyrin repeats. Circles indicate the α helices with their helix axes perpendicular to the plane of the figure. Residue numbers at the start and the end of each secondary structure element are indicated. For the third repeat, solid arrows indicate backbone hydrogen bonds, whereas dashed arrows indicate side-chain hydrogen bonds. A conserved histidine on the α helix that makes a pair of hydrogen bonds to the β -hairpin backbone of the next repeat, contributing to inter-repeat stabilization, is indicated for the second repeat (His³⁶⁵). The first repeat does not have a β hairpin, in part because there is no previous repeat to stabilize it, and the last repeat has an extended helix which is packing against the SH3 domain. (B) The four ankyrin repeats of 53BP2 are aligned according to their structure. Arrows and rectangles indicate the approximate positions of the β strands and α helices, respectively. Their exact positions are indicated by underlining. Residues conserved in two, or more, repeats are highlighted in yellow. (C) p53's L2 loop (blue), which is interrupted by the short H1 helix, and 53BP2's fourth ankyrin repeat (purple) interact through van der Waals contacts, a backbone-backbone hydrogen, and two backbone-side chain hydrogen bonds (yellow dotted lines). Interacting residues are labeled.

teins, including the p16 (INK4) cyclin-dependent kinase4 inhibitor (18), the GABP transcription factor (19), and the notch receptor (20), and such versatility in binding is consistent with the non-globular tertiary structure of the ankyrin motif revealed in our study. The concave and convex surfaces of the L-shaped structure, coupled to the protruding tips of the β hairpin and of the α helices may well offer many possibilities for interactions with diverse macromolecular surfaces.

To investigate further the correlation between tumorigenic mutations and loss of 53BP2 binding, we tested the six most frequently observed p53 mutants and found that they are all defective in 53BP2 binding in vitro (Fig. 5). Four of these mutations (R175H, G245S, R249S, and R282W) involve residues that play important roles for the structural integrity of the conserved surface of p53 (15), and failure by these mutants to bind to 53BP2 is likely due to structural defects; the remaining two mutations (R248W and R273H) involve surface residues that play a role in 53BP2 binding, and failure by these mutants to bind to 53BP2 is likely due to the loss of intermolecular contacts. We also tested the relatively infrequent V143A mutation, which occurs in the hydrophobic core of the β sandwich of p53 (15) and results in a temperature-sensitive phenotype for tumor suppression (21), and found that this mutation eliminated 53BP2 binding at the nonpermissive temperature but not at the permissive temperature (Fig. 5).

Failure by these tumor-derived mutants to bind to 53BP2 closely parallels their

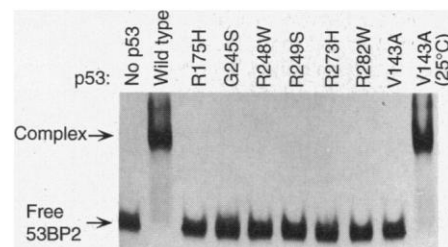


Fig. 5. The six p53 mutants most frequently observed in tumors fail to bind to 53BP2 as determined by the native gel mobility shift assay. Binding reactions contained 30 μ M 53BP2 protein and 1.5 times molar excess of either the wild type or the indicated mutants of the p53 core domain. The binding was performed in 300 mM NaCl at 37°C for 5 min., except for V143A binding at the permissive temperature, which was done at 25°C. Free and p53 bound 53BP2 were separated on a 4.5% polyacrylamide gel in a buffer of 89 mM Tris-borate, pH 8.4, and were visualized with Coomassie staining. The p53 core domain does not enter the gel, presumably because of its net positive charge. The mutant p53 core domains were constructed by PCR mutagenesis and were sequenced.

failure to bind to DNA (15), which is expected because the 53BP2 and DNA binding surfaces and residues of p53 overlap considerably. This raises the possibility that the disruption of 53BP2 binding by tumorigenic mutations may be secondary to their disruption of DNA binding, and loss of 53BP2 binding may thus have little or no functional consequence for tumorigenesis. We note, however, that among the p53 surface residues with no apparent structure-stabilizing roles, those that contact 53BP2 but not DNA (15) are also found mutated, although at lower frequencies [0.3, 0.7, 0.2, and 0.2 percent of the 3393 missense mutations in the database (22) for His¹⁷⁸, Arg¹⁸¹, Met²⁴³, and Asn²⁴⁷, respectively]; and, conversely, those residues that contact only the DNA but not 53BP2 also show similarly low mutational frequencies (0.0, 1.1, 0.6, 1.4, and 0.5 percent for Lys¹²⁰, Ser²⁴¹, Cys²⁷⁷, Arg²⁸⁰, and Arg²⁸³, respectively). In fact, the highest mutational frequencies occur at residues involved in both DNA and 53BP2 binding (8.6 and 8.8 percent for Arg²⁴⁸ and Arg²⁷³, respectively).

The structure provides evidence that the 53BP2-p53 complex forms in vivo. (i) The 53BP2 SH3 domain contains a rare amino acid substitution (Leu⁵¹⁴) at an otherwise strictly conserved residue of the SH3 consensus, and this substitution appears to be critical for p53 binding. (ii) The fourth ankyrin repeat contains an insertion (Tyr⁴²⁴) compared to the ankyrin consensus, and the insertion is critical for the surface complementarity at the ankyrin-p53 interface. (iii) The p53 surface that interacts with 53BP2 is highly conserved across species and is frequently mutated in cancer. (iv) The p53 surface residues that contact 53BP2 but not DNA are also mutated in cancer.

Little is known about the cellular role of the 53BP2, whose complete coding region of 1005 amino acids has only recently been described (23). One report indicates that 53BP2 also binds the bcl2 apoptosis inhibitor in vitro (23), and coupled to the observation that transactivation may not be required for p53-induced apoptosis (5), points to a possible role for 53BP2 in apoptosis. Conversely, there are other roles consistent with available data. For example, neuroblastomas and breast carcinomas often contain wild-type p53 that is excluded from the nucleus (24), suggesting that a component of the p53 pathway, possibly a component that interacts with p53, may be altered in these cases. These and other possible roles for 53BP2 can now be directly assessed through the use of mutations at p53 residues that contact 53BP2 but not DNA, as revealed by the crystal structure of the 53BP2-p53 complex.

REFERENCES AND NOTES

- L. J. Ko and C. Prives, *Genes Dev.* **10**, 1054 (1996).
- M. S. Greenblatt, W. P. Bennett, M. Hollstein, C. C. Harris, *Cancer Res.* **54**, 4855 (1994).
- M. B. Kastan *et al.*, *Cell* **71**, 587 (1992); Y. Yin, M. A. Tainsky, F. Z. Bischoff, L. C. Strong, G. M. Wahl, *Cell* **70**, 937 (1992); L. R. Livingstone *et al.*, *Cell* **70**, 923 (1992).
- H. Symonds *et al.*, *Cell* **78**, 703 (1994); H. Hermeking and D. Eick, *Science* **265**, 2091 (1994); X. Wu and A. J. Levine, *Proc. Natl. Acad. Sci. U.S.A.* **91**, 3602 (1994); P. Sabbatini, J. Lin, A. J. Levine, E. White, *Genes Dev.* **9**, 2184 (1995).
- C. Caelles, A. Heimberg, M. Karin, *Nature* **370**, 220 (1994).
- W. S. El-Deiry, S. E. Kinzler, J. A. Pietenpol, K. W. Kinzler, B. Vogelstein, *Nature Gen.* **1**, 45 (1992); S. E. Kern *et al.*, *Science* **252**, 1708 (1991).
- G. Farmer *et al.*, *Nature* **358**, 83 (1992); S. E. Kern *et al.*, *Science* **256**, 827 (1992).
- W. S. El-Deiry *et al.*, *Cell* **75**, 817 (1993); J. W. Harper, G. R. Adami, N. Wei, K. Keyomarsi, S. J. Elledge, *Cell* **75**, 805 (1993).
- C. Deng, P. Zhang, J. W. Harper, S. J. Elledge, P. Leder, *Cell* **82**, 675 (1995); J. Brugarolas *et al.*, *Nature* **377**, 552 (1995).
- L. A. Donehower *et al.*, *Nature* **356**, 215 (1992).
- K. Iwabuchi, P. L. Bartel, B. Li, R. Marraccino, S. Fields, *Proc. Natl. Acad. Sci. U.S.A.* **91**, 6098 (1994); S. K. Thukral, G. C. Blain, K. H. Chang, S. Fields, *Mol. Cell. Biol.* **14**, 8315 (1994).
- Goat antibody to GST coupled to the CM5 sensor chip (BIAcore) was used for the binding of the 53BP2-GST fusion protein. The p53 core domain protein at 10, 40, 60, 80, and 100 nM concentrations was injected onto the chip in 100 mM NaCl for 2 min. followed by 2 min. of dissociation phase. The binding data were analyzed by means of the BIAevaluation software.
- P. Michaely and V. Bennett, *Trends Cell Biol.* **2**, 127 (1992).
- G. B. Cohen, R. Ren, D. Baltimore, *Cell* **80**, 237 (1995).
- Y. Cho, S. Gorina, P. D. Jeffrey, N. P. Pavletich, *Science* **265**, 346 (1994).
- H. Yu *et al.*, *Cell* **76**, 933 (1994); W. A. Lim, F. M. Richards, R. O. Fox, *Nature* **372**, 375 (1994).
- X. Wu *et al.*, *Structure* **3**, 215 (1995).
- M. Serrano, G. J. Hannon, D. Beach, *Nature* **366**, 704 (1993).
- C. C. Thompson, T. A. Brown, S. L. McKnight, *Science* **253**, 253 (1991).
- M. E. Fortinini and S. A. Tsakonas, *Cell* **79**, 273 (1994).
- D. Michalovitz, O. Halevy, M. Oren, *ibid.* **62**, 671 (1990).
- Database of p53 mutations, European Molecular Biology Laboratory Data Library (1995).
- L. Naumovski and M. L. Cleary, *Mol. Cell. Biol.* **16**, 3884 (1996).
- U. M. Moll, M. L. Quaglia, J. Bénard, G. Riou, *Proc. Natl. Acad. Sci. U.S.A.* **92**, 4407 (1995); U. M. Moll, G. Riou, A. J. Levine, *ibid.* **89**, 7262 (1992).
- The GST-53BP2 fusion protein [53BP2 residues 291 to 529; numbering according to (13)] was overexpressed in *Escherichia coli* (11). 53BP2 was cleaved from the fusion protein by factor Xa, and it was purified by anion exchange and gel filtration chromatography. The complex was formed by mixing the 53BP2 preparation with the p53 core domain [residues 94 to 292, (15)], and it was concentrated by ultrafiltration to 20 mg/ml in a buffer of 50 mM bis-tris propane-HCl (BTP), 200 mM NaCl, 5 mM dithiothreitol (DTT), pH 6.8. Crystals were grown at 4°C by the hanging drop vapor diffusion from 10% polyethylene glycol (PEG) 8000, 8% ethylene glycol, 100 mM Hepes, 300 mM KCl, 10 mM DTT, pH 7.5. The crystals form in space group $P2_12_12_1$ with $a = 68.7$, $b = 72.3$, $c = 118.1$ Å and contain one complex in the asymmetric unit. Diffraction data were collected at -170°C with crystals flash frozen in crystallization buffer containing 30% ethylene glycol. The native-1 and derivative data sets were collected with the R-AXISIIc imaging plate detector mounted on a Rigaku

200HB generator. The native-2 data set was collected with a CCD detector at the A1 beamline of the Cornell High Energy Synchrotron Source (MacCHESS). The structure was determined by a combination of multiple isomorphous replacement (MIR) and molecular replacement (MR) methods. The position of the p53 core domain was determined by molecular replacement (MR) with the program X-PLOR (26), and the structure of the core domain from the p53-DNA complex (15). The correlation coefficient was 0.45 for 10 Å to 4 Å data. Heavy atom soaks were performed in well buffer lacking DTT, containing either 0.5 mM HgCl₂ or 0.5 mM lead acetate, for 4 and 24 hours, respectively. The MIR analysis with the CCP4 program suite (27) included anomalous scattering from the HgCl₂ derivative and had a mean figure of merit of 0.50 for 20.0 Å to 3.2 Å data. Initial maps were calculated by combining the MIR and the MR p53 phases with the program SIGMAA (27) and showed interpretable density for 53BP2. Successive rounds of model building, simulated annealing refinement with the program X-PLOR and phase combination allowed the complete interpretation of the 53BP2 structure. The model was then further refined by least squares refinement with the program TNT (28). In the crystals, the 53BP2 molecule has an overall temperature factor of 64.0 Å², which is significantly higher than that of the p53 core domain (35.0 Å²). Consequently, the overall 53BP2 electron density is of lower quality than that of p53. The final model consists of residues 97 to 287 of

p53, residues 327 to 519 of 53BP2 and 275 water molecules. 53BP2 residues 291 to 326 from the NH₂-terminus, residues 491 to 495 of the n-src loop of the SH3 domain, and residues 436 to 441 in the linker between the α helices of the fourth ankyrin repeat have poor electron density and are likely to be disordered in the crystals.

26. A. T. Brunger, *X-PLOR, a system for crystallography and NMR, Version 3.0 Manual* (Yale Univ. Press, New Haven, CT 1991).
27. Collaborative Computational Project, No. 4. *Acta Crystallogr.* **D50**, 760 (1994).
28. D. E. Tonrud, L. F. Ten Eyck, B. W. Matthews, *ibid.* **A43**, 489 (1987).
29. We thank S. Fields for providing us with the 53BP2 expression plasmid; the staff of the Cornell High Energy Synchrotron Source MacChess for help with data collection; S. Geromanos of the Sloan-Kettering Microchemistry Facility for NH₂-terminal sequence analyses; W. Farley for help with the surface plasmon resonance experiments; M. Mayhew for helpful discussions; and R. Kenny for administrative assistance. Supported by the NIH (CA65698), the Pew Charitable Trusts, the Arnold and Mabel Beckman Foundation, the Dewitt Wallace Foundation, and the Samuel and May Rudin Foundation. Coordinates have been deposited with the Brookhaven Protein Data Bank (code 1YCS).

28 May 1996; accepted 5 September 1996

U1-Mediated Exon Definition Interactions Between AT-AC and GT-AG Introns

Qiang Wu and Adrian R. Krainer*

A minor class of metazoan introns has well-conserved splice sites with 5'-AU-AC-3' boundaries, compared to the 5'-GU-AG-3' boundaries and degenerate splice sites of conventional introns. Splicing of the AT-AC intron 2 of a sodium channel (SCN4A) precursor messenger RNA *in vitro* did not require inhibition of conventional splicing and required adenosine triphosphate, magnesium, and U12 small nuclear RNA (snRNA). When exon 3 was followed by the 5' splice site from the downstream conventional intron, splicing of intron 2 was greatly stimulated. This effect was U1 snRNA-dependent, unlike the basal AT-AC splicing reaction. Therefore, U1-mediated exon definition interactions can coordinate the activities of major and minor spliceosomes.

Precursor mRNA (pre-mRNA) splicing requires the stepwise assembly of the U1, U2, U4/U6·U5 small nuclear ribonucleoprotein (snRNP) particles, and numerous proteins on the substrate to form a spliceosome, which catalyzes two sequential trans-esterification reactions (1). Most introns have 5' and 3' splice sites that match degenerate consensus sequences, of which the 5'-GT and AG-3' intron ends are nearly invariant features. Many point mutations that result in a variety of human genetic diseases affect these dinucleotides and seriously impair gene expression (2). Mutation of G to A at the 5' end or of G to C at the 3' end is especially deleterious, but the double mutation restores splicing (3). Recently, a minor

class of natural pre-mRNA introns with 5'-AT and AC-3' boundaries emerged as an exception to the GU-AG rule (4, 5) (Table 1). The mouse cyclin-dependent kinase CDK5 and the human voltage-gated skeletal muscle and cardiac muscle sodium channel α subunits (SCN4A and SCN5A) also contain AT-AC introns (Table 1) (6).

Most AT-AC introns share highly conserved sequences at the 5' splice site, at the presumptive branch site, and a shorter sequence at the 3' splice site (Table 1). They lack the extensive polypyrimidine tract characteristic of most conventional 3' splice sites, and the distance between the presumptive branch site and the 3' splice site junction is unusually short. Intron 21 of human SCN4A and intron 25 of human SCN5A, which interrupt homologous positions of the coding sequence, also begin with AT and end with AC; however, the rest of their 5' splice site and putative

branch site sequences does not match the consensus, which may indicate that these two introns belong to a distinct subclass of AT-AC introns. There are no obvious structural relations or common expression patterns among the genes or gene families that contain AT-AC introns, and neither the length nor the position of AT-AC introns is conserved among unrelated genes. However, AT-AC introns and their positions within specific genes are conserved phylogenetically. Two members of the gene family of voltage-gated sodium channels, SCN4A and SCN5A, contain AT-AC introns at homologous positions, and it is likely that these introns will prove to be conserved in other sodium and perhaps calcium channel family members (7).

A pre-mRNA consisting of the SCN4A AT-AC intron 2, the two flanking exons, and nine nucleotides (nt) of the conventional intron 3 (Fig. 1) was transcribed *in vitro* (8). Optimal conditions for splicing of this substrate in HeLa cell nuclear extracts were established (9). The maximal splicing efficiency was 11% (Fig. 1A). SCN4A spliced less efficiently and with much slower kinetics than β-globin. The extent of splicing did not increase beyond 6 hours (10). The fidelity of splicing was verified by sequencing of the gel-purified mRNA after reverse transcriptase-polymerase chain reaction (RT-PCR) amplification (10, 11). In addition to the major AT-AC spliced product, a minor product accumulated that corresponds to conventional GT-AG splicing by means of cryptic 5' and 3' splice sites located in exons 2 and 3, respectively (Fig. 1B), as verified by sequencing (10, 11). RNA molecules corresponding to free exon 2 and lariat-exon 3 intermediates, and to released intron lariat, also appeared with appropriate kinetics (Fig. 1A). As expected, the lariat molecules had anomalously slow mobility on higher percentage gels (10, 12).

Recently, accurate *in vitro* splicing of the human P120 AT-AC intron was reported and could only be detected upon debilitation of U1 or U2 snRNPs with complementary 2'-O-methyl oligonucleotides (13). Because efficient accessibility of snRNPs requires incubation with adenosine triphosphate (ATP) (14), this approach precluded a study of the ATP requirement for AT-AC splicing. Because SCN4A AT-AC splicing can be detected in untreated extracts (Fig. 1A), we examined the requirement for ATP and magnesium and found that both are essential for AT-AC splicing (10).

To examine the role of major and minor snRNPs in SCN4A AT-AC splicing *in vitro*, we used oligonucleotide-directed ribonuclease H (RNase H) cleavage of the snRNAs (14), and the resulting extracts

Cold Spring Harbor Laboratory, Post Office Box 100, Cold Spring Harbor, NY 11724-2208, USA.

*To whom correspondence should be addressed. E-mail: krainer@cshl.org